Chemical Engineering Science 161 (2017) 215–227

Contents lists available at ScienceDirect

Chemical Engineering Science

journal homepage: www.elsevier.com/locate/ces

On the effect of surfactants on drop coalescence at liquid/liquid interfaces

Weheliye Hashi Weheliye, Teng Dong, Panagiota Angeli *

Chemical Engineering Department, University College London, Torrington Place, WC1E 7JE, UK

ARTICLE INFO

Article history:
Received 28 August 2016
Received in revised form 11 November 2016
Accepted 1 December 2016
Available online 12 December 2016

Keywords:
Coalescence
Liquid/liquid interface
Surfactant
Vorticity
Kinetic energy per unit mass

ABSTRACT

In this work the effect of surfactants on the coalescence of a drop with a flat aqueous-organic interface was experimentally investigated. A high speed Particle Image Velocimetry (PIV) system was used to obtain velocity profiles and kinetic energy per unit mass distribution inside the coalescing droplets. Different mass ratios of surfactant to oil below the CMC value, up to $\phi = 5 \times 10^{-4}$, of a non-ionic surfactant dissolved in the organic phase were studied. It was found that an increase in the surfactant concentration promoted the deformation of the interface before the film that separated the drop from the interface ruptured. A high surfactant concentration also increased the time needed for film rupture. When rupture occurred, two counter-rotating vortices formed inside the droplet on either side of the rupture point, which moved upwards with time. The propagation of the vortices inside the droplet was faster for low surfactant concentrations, while the intensities of the two counter-rotating vortices significantly decreased for increasing surfactant concentration. At the early stages of coalescence after film rupture, the kinetic energy per unit mass was mainly distributed near the bottom part of the droplet, while at later stages it was distributed near the upper part of the droplet.
© 2016 The Authors. Published by Elsevier Ltd. This is an open access article under the CC BY license (http://creativecommons.org/licenses/by/4.0/).

1. Introduction

Drop coalescence is commonly encountered in daily life, for example in the formation of rain drops or the merging of dewdrops in leaves. It is also a very important phenomenon in a wide range of industrial applications in food processing and in chemical, petroleum and pharmaceutical fields (Paul et al., 2004). In food emulsions (such as milks and coffee creamers), the droplets should remain stable for the whole life of the products and coalescence should be prevented. However, during processing of dairy products such as ice-creams or whipping creams, droplets need to coalesce easily and quickly. In food emulsions, the drop surface is always coated with surfactants, whose properties largely affect the coalescence behavior (Dalgleish, 1997). In current oil extraction approaches, water is injected into the well to displace the residual oil in rock gaps and enhance the crude oil recovery. During injection, oil-water dispersions form. In some cases, surfactants are also added to facilitate the formation of the dispersions. Previous studies have shown that the oil recovery efficiency is affected by the addition of surfactants. As it is difficult to trace the distribution of the surfactants along the droplet surface, the effect of surfactants on the coalescence process is still an active research area (Samanta and Ghosh, 2011; Lu and Corvalan, 2012). In industrial applications coalescence occurs in complex environments with many drops present. Multiple coalescence events may occur among drops or between drops and interfaces. To be able to study in detail the various steps of the coalescence process, in this paper, the coalescence of a single drop with an interface is investigated in the presence of surfactants.

The process and dynamics of coalescence have been investigated extensively previously. It is generally accepted that the coalescence process involves four consecutive stages; i.e. collision of liquid bodies, drainage of the thin film trapped between them, rupture of the thin film, and merging of the liquid bodies (Paul et al., 2004; Aarts and Lekkerkerker, 2008; Liao and Lucas, 2010). After collision, a period of time, which is called the drainage time or drop rest time, is needed for the trapped film to drain out. When the film between the coalescing bodies drains to a thickness of about ≈100 nm, van der Waals forces become significant and cause the film rupture (Chen, 1985). Film rupture has recently been studied using different advanced experimental techniques (Aarts and Lekkerkerker, 2008; Malmazet et al., 2015; Eri and Okumura, 2010; Mohamed-Kassim and Longmire, 2004). The investigations mainly focused on the locations of the rupture points and the retracting velocity of the meniscus connecting the two coalescing bodies after film breakage. The rupture occurs at the thinnest part of the film, which can be at or off center. Charles and Mason (1960)

* Corresponding author.
E-mail address: p.angeli@ucl.ac.uk (P. Angeli).

http://dx.doi.org/10.1016/j.ces.2016.12.009
0009-2509/© 2016 The Authors. Published by Elsevier Ltd.
This is an open access article under the CC BY license (http://creativecommons.org/licenses/by/4.0/).

Nomenclature

Abbreviation

2D	Two-Dimensional
CMC	Critical Micelle Concentration
PIV	Particle Image Velocimetry

Greek symbols

$\Gamma_{\omega_z^*}$	space average of the circulation intensity for the time-resolved flow field, s^{-1}
γ	interfacial tension, mN/m
λ	fluid viscosity ratio, –
μ	dynamic viscosity, kg s^{-1} m^{-1}
ρ_d	density of the droplet fluid, kg/m^3
ρ_s	density of the surrounding fluid, kg/m^3
ρ_m	average density, kg/m^3
ϕ	mass ratio of surfactant to organic phase, –
ω_z	vorticity components in the z direction, s^{-1}

Roman symbols

Bo	bond number, –
Bo_R	bond number based on the radius of the droplet, –
D	droplet diameter, m
h_s	relative height from the equilibrium interface, m
k_{xy}	kinetic energy per unit mass estimated from the x and y velocity components, m^2/s^2
k^*_{xy}	space average of the kinetic energy per unit mass of the entire droplet, m^2/s^2
Oh	Ohnesorge number, –
R	droplet radius, m
t	droplet receding time, s
u	radial velocity, m/s^1
v	vertical velocity, m/s^1

and Neitzel and Dell'Aversana (2002) listed three types of rupture, i.e. (a) central rupture (b) off-center rupture (c) double rupture. The off-center rupture occurs more often than the central rupture, while the double rupture is much less common than the other two types. The rupture locations can also be greatly influenced by surrounding droplets or particles (Bordoloi and Longmire, 2012).

Following the film rupture, two main regimes have been identified for the expansion of the neck which connects the two coalescing bodies. These regimes are characterized by different scaling laws, depending on whether the viscous or inertial forces are dominant in resisting the surface tension forces that drive the coalescence. The scaling developed by Aarts et al. (2005) states that when the neck of the bridge is sufficiently small, immediately after film rupture, viscous forces dominate. In this regime, the Capillary number can be taken equal to $Ca = \mu V_{visc}/\gamma = 1$ and the neck velocity is estimated as $V_{visc} = \gamma/\mu$. The cross-over from the viscous to the inertial regime for film rupture will happen at Reynolds numbers (based on the neck radius as the characteristic length and on the neck velocity of the viscous regime) close to 1. This leads to a crossover time from the viscous to the inertial regime at $t_n = \mu^3/\rho\gamma^2$. It should be noted that the velocity by which the neck radius grows remains constant throughout the viscous regime, $V_{visc} = \gamma/\mu$, while in the inertial regime the neck radius grows with a velocity, $V_{iner} = \frac{1.2}{\sqrt{t}}\left(\frac{R\gamma}{\rho}\right)^{1/4}$.

As noted by Kavehpour (2015), in recent years cascade coalescence dynamics have been investigated widely, where a secondary droplet appears after the coalescence which also coalesces and may produce another droplet (Thoroddsen and Takehara, 2000; Gilet et al., 2007; Martin and Blanchette, 2015). This phenomenon is characterized by the dimensionless Ohnesorge number, $Oh = \frac{\mu\sqrt{\rho_m}}{\rho\sqrt{\gamma R}}$, where ρ_m is the average density of the two fluids, and the Bond number, $Bo_R = \Delta\rho g R^2/\gamma$, based on the radius of the droplet. Gilet et al. (2007) plotted a phase map to show the partial coalescence and total coalescence regions in terms of two Ohnesorge numbers $Oh_1 = \frac{\mu_1\sqrt{\rho_m}}{\rho\sqrt{\gamma R}}$ and $Oh_2 = \frac{\mu_2\sqrt{\rho_m}}{\rho\sqrt{\gamma R}}$ based on the aqueous and the organic phase, respectively. Partial coalescence was observed in the phase map when $Oh_1 < 0.03$, $Oh_2 < 0.2$ and $Bo_R < 0.1$. In addition to this, Martin and Blanchette (2015) reported that the presence of surfactant can lower the critical Ohnesorge number for partial coalescence by more than 30%.

In many applications, surfactants are added to stabilize the dispersions and their effects on coalescence have been studied extensively. Surfactants can affect all stages of the coalescence from the interface deformation during the rest time, to film drainage and to the merging of the coalescing bodies. It has been found that the droplet rest time becomes longer when even small amounts of surfactants are present which has been attributed to Marangoni backflow (Blawzdziewicz et al., 1999). However, Ghosh and Juvekar (2002) argued that Marangoni flow does not occur because the surfactant molecules generating the Marangoni forces are displaced by the lubrication forces in the film at the initial stages of droplet resting. The only effect of surfactants is to suppress the circulation inside the droplet and increase the rigidity of the drop interface. A new model was derived to predict the coalescence time distribution by analyzing the surfactant concentration along the droplet surface. Dai and Leal (2008) numerically analyzed the effect of surfactants on rest time for drop-drop coalescence. Using Langmuir isotherms to link the interfacial tension to surfactant concentration along the drop surface, it was possible to calculate surfactant concentration profiles. The tangential velocity along the drop surface and the deformation of the film shape were also analyzed. The authors discussed that the Marangoni stresses decreased significantly the tangential velocity and suppressed the drop surface mobility but had little influence on the velocity in the thin film region. Blanchette et al. (2009) investigated numerically the partial coalescence of droplets with a flat interface and found that when the surface tension of the droplet and the interface differed, the region of higher surface tension pulled the interface and generated tangential motion so that the surface of the high surface tension liquid was covered with low surface tension liquid. In recent numerical investigations of a drop with a flat interface, Martin and Blanchette (2015) showed that the transition from total to partial coalescence depended on the surfactant distribution on the interfaces. In agreement with experimental observations, the interface was found to deform drastically when

Table 1
Fluid properties.

	ρ [kg/m^3]	μ [mPa s]	γ [mN/m]	ϕ [–]
Water/glycerol	1210	54	–	21% v/v
Exxsol D80/Span80	804	1.75	26.73	0 w/w
			23.43	2×10^{-5} w/w
			13	1×10^{-4} w/w
			7.8	2×10^{-4} w/w
			2.16	5×10^{-4} w/w

surfactants are present, which affects the distribution of surfactants along the drop surface.

The complex motion of surfactants at the interfaces during coalescence is affected by the velocity fields generated inside and outside the dorplet. Velocity fields have been obtained numerically in some cases but there are very few experimental studies available where velocity fields inside the coalescing bodies are obtained with Particle Image Velocimetry (PIV) (Mohamed-Kassim and Longmire, 2004; Ortiz-Dueñas et al., 2010; Bordoloi and Longmire, 2012; Chinaud et al., 2016). Earlier studies by Mohamed-Kassim and Longmire (2004) on drop coalescence with a flat interface, captured the evolution of the vertical and radial velocities inside the droplets at different drop-ambient viscosity ratios $\lambda = 0.14$ and 0.33. At first, the collapsing liquid in the drop

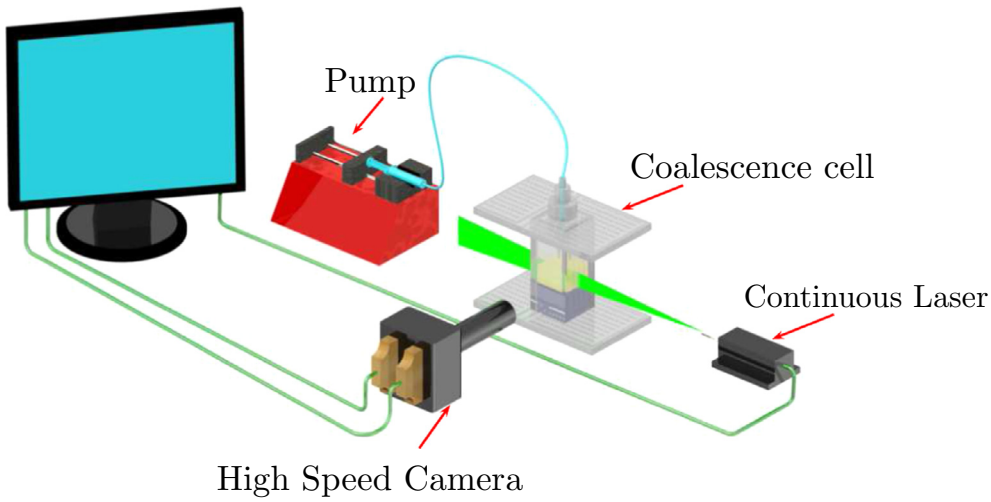

Fig. 1. Sketch of the experimental set up and the PIV system used to investigate the coalescence process.

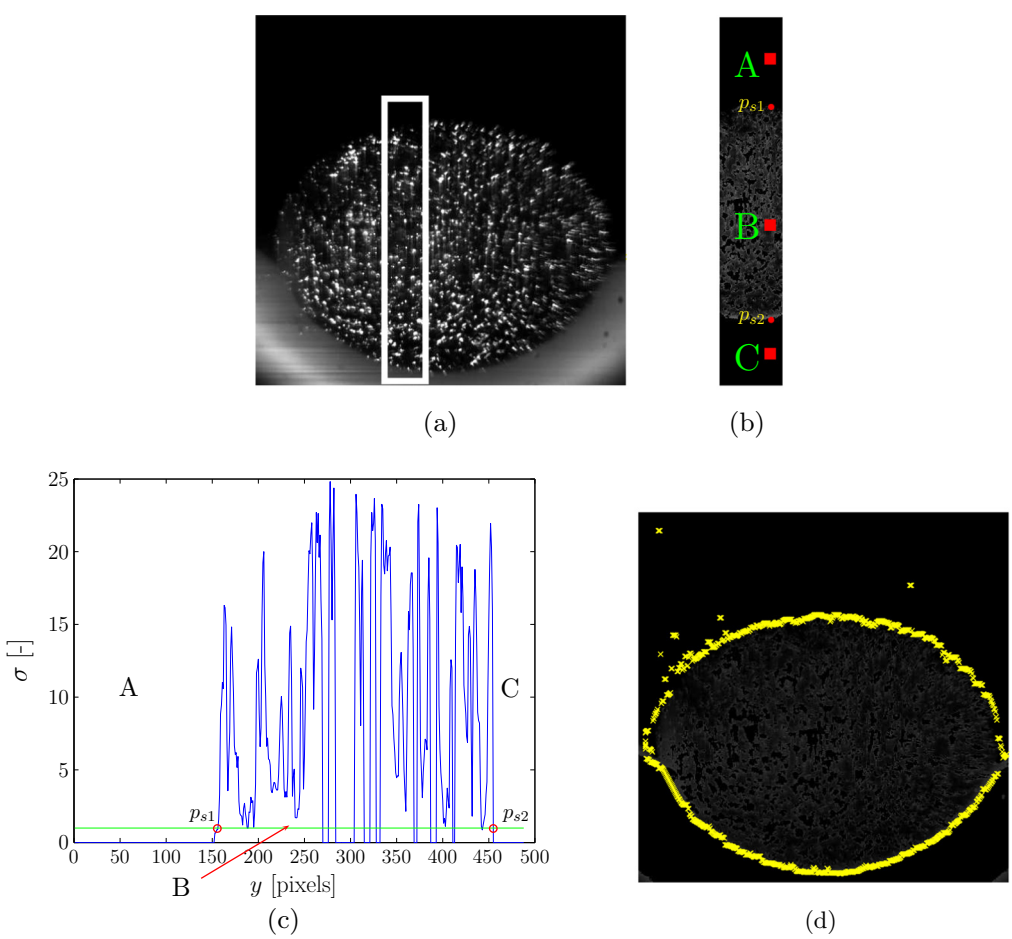

Fig. 2. Description of the steps in the detection algorithm of the droplet profile: (a) identification of laser reflections at the organic-aqueous interface; (b) close up region enclosed in the white rectangle to show three different positions in the estimation of σ; (c) variation of σ along a vertical height of the droplet; (d) raw profile of the droplet surface detected after the standard deviation analysis.

near the breaking film generated two dominant vortices inside the drop, whose intensities varied with λ. The vortices moved upwards along the drop inner surface and gradually contracted. In later studies (Bordoloi and Longmire, 2012), tomographic PIV was used to investigate the effects of neighboring particles on drop coalescence and showed that the particles shift the rupture point and lead to asymmetry of the velocity field inside the droplet. In a recent work by Chinaud et al. (2016), bright field PIV was used to study the early stages of coalescence in a two-dimensional Hele-Shaw cell.

When surfactants are present, they distribute along the interfaces. In drop-interface coalescence the uneven distribution of surfactants can deform the interface and change the tangential stresses. These two factors affect the velocity fields inside the droplet and influence the coalescence time. The aim of this paper is to investigate the evolution of the coalescence between a drop and an interface in a three-dimensional configuration in the presence of surfactants and to determine hydrodynamic properties such as interface characteristics, velocity and vorticity fields and kinetic energy per unit mass inside the drops.

2. Experimental setup

This section provides a detailed description of the experimental set up and the PIV system used for the investigation of drop coalescence with a flat interface between two immiscible liquids in the presence of surfactants. The experimental set up and the working principles of the PIV are described in Section 2.1. The procedure developed to track the shape of the droplet profile for a given time instant is reported in Section 2.2, whilst the limitations of the experiments are assessed in Section 2.3.

2.1. Materials and methodology

The mechanism of coalescence of a drop with a liquid-liquid interface and the evolution of the velocity and vorticity fields inside the drop were investigated with 2D Particle Image Velocimetry. The experiments were conducted in a transparent acrylic tank of 50 mm square section width and 150 mm height. The aqueous phase, a mixture of water (79%)-and glycerol (21%) was placed at the bottom of the tank up to a height of 40 mm and the oil phase was placed on top of it with a height of 60 mm oil. The liquid properties are given in Table 1. To eliminate optical distortions in the PIV measurements, the refractive indices of the water-glycerol and Exxsol D80 were matched. Refractive indices were measured with a refractometer (Abbe 5, BS) and were found to be r_{ExD80} = 1.443 (20 °C) for Exxsol D80 and $r_{wat:gly}$ = 1.443 (20 °C) for the aqueous phase. Droplets of water-glycerol mixture with an equivalent diameter of $D \approx 4$ mm were generated by injecting the liquid into the Exxsol D80 through a cylindrical nozzle of 80 mm length and 2 mm diameter. The nozzle was fixed approximately 20 mm above the oil-water interface to prevent the variation of the droplet impact locations. For the investigation of the velocity fields the droplets were seeded with 1 μm Rhodamine coated spherical particles. These particles were removed from the interface with a suction pump after each experiment to improve the quality of the images near the organic-aqueous interface. In addition, to improve the interface imaging the bulk aqueous phase was dyed with a small amount of Rhodamine 6G.

For the surfactant studies, Span 80 was introduced into the organic phase, which is an oil soluble and non-ionic surfactant with HLB = 4.3. Five different surfactant concentrations were tested, with mass ratios of surfactant to organic phase of $\phi = 0$, $\phi = 2 \times 10^{-5}$, $\phi = 1 \times 10^{-4}$, $\phi = 2 \times 10^{-4}$ and $\phi = 5 \times 10^{-4}$. The interfacial tensions under different concentrations were measured with the Du Nouy ring method. As can be seen from Table 1, the interfacial tension decreases with increasing surfactant concentration but changes less close to the CMC concentration, at $\phi = 5 \times 10^{-4}$. The presence of the Rhodamine 6G or the tracer particles in the aqueous phase did not affect the interfacial tension values (variation of less than 5%).

The 2D PIV system employed in this study consists of a continuous diode laser, a cylindrical lens, and a high speed camera. The laser has an output power of 300 mW with a wavelength of 532 nm and 4 mm beam size. A cylindrical lens was mounted in front of the laser to create a laser light sheet of approximately 1 mm thickness. A schematic diagram of the PIV system set up

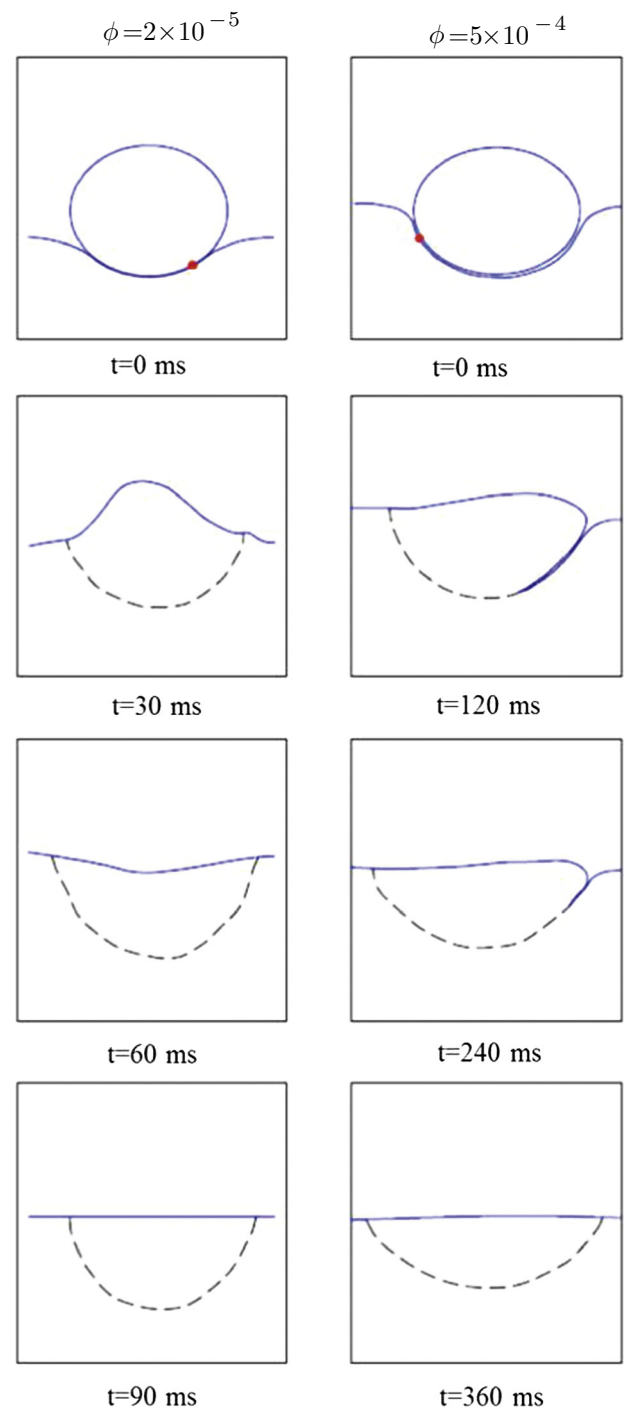

Fig. 3. Time evolution of the drop before and after film rupture for $\phi = 2 \times 10^{-5}$ and $\phi = 5 \times 10^{-4}$.

for the measurements on a vertical plane in the acrylic vessel is provided in Fig. 1. The high speed camera (Photron APX) was equipped with a mono-zoom Nikkon lens, which gave a field of view of $9 \times 9\ \mathrm{mm}^2$. The images obtained from the PIV measurements were treated with the freeware package JPIV. An adaptive correlation analysis of the full image was applied with a final interrogation window of 32×32 pixels. A 50% window overlap was used for a final resolution of 16×16 pixels, corresponding to an area of $0.14 \times 0.14\ \mathrm{mm}^2$. The number of images obtained for each experiment varied between 500 and 1000, while the image acquisition frame rates were set from 333.3 Hz to 1 kHz (Δt = 1–3 ms). It should be noted that all the experiments in this work were conducted at room temperature.

2.2. Droplet shape tracking algorithm

An image analysis algorithm comprising of three steps was developed to identify the profile of the droplet shape at a given time instant. In the first step, the bottom part of the PIV image, at the bulk of the aqueous phase, was made uniform, by removing any reflections of the laser light at the interface. In this case, every pixel with a light intensity $i > 0.5$ (where an intensity value $i = 1$ indicates white) was converted to an intensity value of 0 (i.e. black). In the second step, the coordinates of the points positioned on the edge of the droplet were determined by exploiting the differences in illumination texture of points above and below the droplet. A close up of the white rectangular region of Fig. 2(a) is shown in Fig. 2(b) where three points above, on and below the droplet are denoted as A, B, and C, respectively. It is evident that points A and C are located in regions with a more uniform illumination texture, while the presence of seeding particles gives an accentuated inhomogeneity of scattered light within the droplet (i.e. point B). To estimate the level of inhomogeneity of the local illumination texture, a window of 3×3 pixels was created around each pixel of the image and the local standard deviation, σ, of the light intensity of the nine points within the window was calculated using Eq. (1).

$$\sigma = \sqrt{\frac{1}{N_w}\sum_{i=1}^{N_w}(i_k - i_m)^2} \tag{1}$$

where N_w is the number of points in the window, i_m is the mean value of the light intensity in the window and i_k is the light intensity of the k_{th} point of the window. The standard deviation was estimated for every pixel of the image. The variation of the standard deviation along the vertical direction, y, at a characteristic axial location x, is shown in Fig. 2(c). The origin of the image is located in the upper left corner, and therefore increasing y corresponds to points further down the image. From Fig. 2(c) it is evident that the value of the standard deviation, σ, is zero at small values of y (i.e. upper part of the image) where most of the image is dark and the local illumination texture is uniform as shown in Fig. 2(b) and point A. As the upper surface of the droplet is approached a sharp increase of σ occurs, because the 9-point interrogation window is across the upper edge of the droplet and a significant difference in light intensity occurs between points above and inside the droplet. With a further increase in y the interrogation window is located completely inside the droplet (point B in Fig. 2(b) and (c)). For $y > 150$ and $y < 460$, the interrogation window is completely inside the seeded droplet region and it varies around a value of 20, because of the light inhomogeneity due to the presence of the seeding particles. A decrease of the value of σ occurs when the

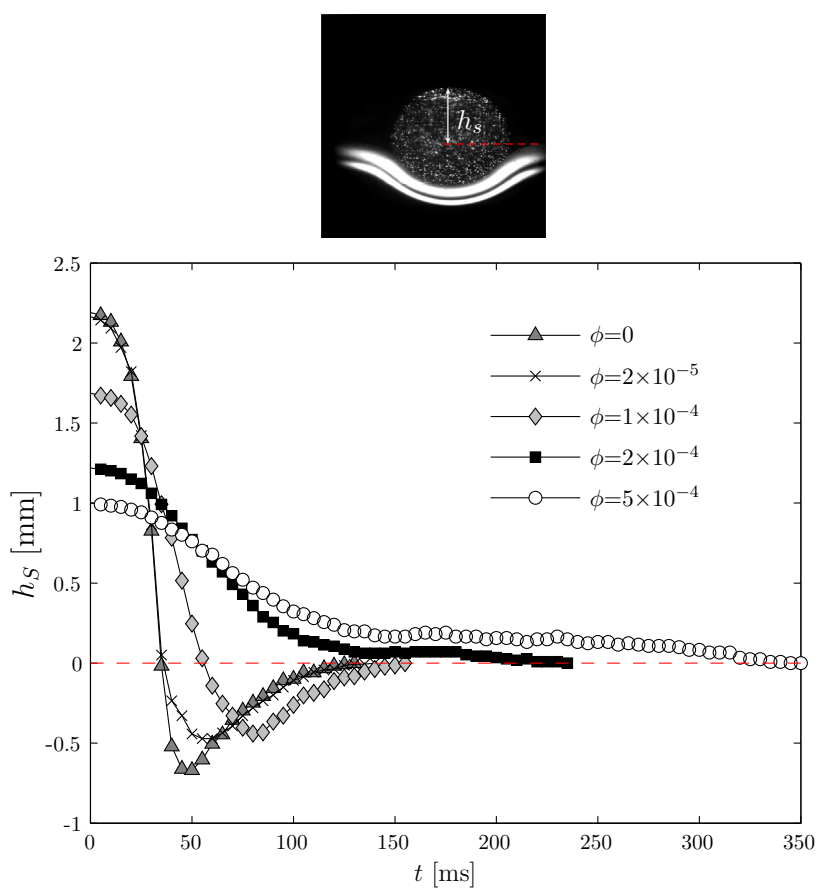

Fig. 4. The variation of the height from the drop upper surface to the equilibrium interface, h_s, with increasing receding meniscus time, t, for a single droplet coalescence event.

interrogation window is across the bottom edge of the droplet at $y > 460$ (lower part of the image, point C). The presence of the first and last peak of σ together with the pronounced noisy texture in between allows the identification of the edges of the upper (p_{s1}) and the lower surface (p_{s2}) of the droplet, respectively. The same procedure was repeated for each horizontal coordinate x until the entire droplet profile at a given time instant was determined, as illustrated in Fig. 2(d). It is evident that the algorithm identifies most of the points on the top and bottom edge of the droplet. The third step involved a local regression to smooth the detected droplet profile, as well as to identify and discard those outliers whose distance from the droplet was greater than a fixed threshold. A mask was then applied to each raw image and the values of all pixels outside the droplet profile were converted into black.

2.3. Experimental limitations

The experimental investigations of velocity fields were conducted for the complete evolution of the coalescence. The PIV system used has a maximum sampling frequency of the order of 1 kHz. Therefore, the time difference between two consecutive images is of the order of 1 ms, which limited the investigation of the high magnitude velocities occurring at the early stages of coalescence in the systems with high interfacial tension, i.e. for no surfactant present or for mass ratio of surfactant to organic phase equal to $\phi = 2 \times 10^{-5}$. For the rest of the discussion, image analysis of the coalescence process was carried out for the whole range of surfactant concentrations while velocity fields were obtained for mass ratio of surfactant to organic phase, $\phi = 1 \times 10^{-4}$, $\phi = 2 \times 10^{-4}$ and $\phi = 5 \times 10^{-4}$.

3. Results

The results section is separated into three parts. In the first part, the evolution of interfacial characteristics and droplet coalescence is investigated. In Section 3.2, the velocity and vorticity fields inside the coalescing droplet and their evolution after film rupture are investigated for three different surfactant concentrations. Furthermore, this section provides an estimate of the circulation and the position of the center of the two counter-rotating vortices inside the droplet during coalescence. The content of the kinetic energy per unit mass inside the droplet is subsequently investigated in Section 3.3 for varying surfactant concentrations.

3.1. Interfacial characteristic and droplet coalescence evolution

The rupture behavior of the droplets at different surfactant concentrations is first analyzed. The aqueous phase drops generated from the nozzle initially rest on the aqueous-organic interface before the film ruptures. From the PIV images it can be seen that during this resting period, the liquid inside the droplet is motionless prior to the rupture. When rupture occurs, the tracer particles close to the rupture point start to move. This instant is defined as the starting point of the rupture, while the moment when the interface returns to the initial quiescent level is recognized as the

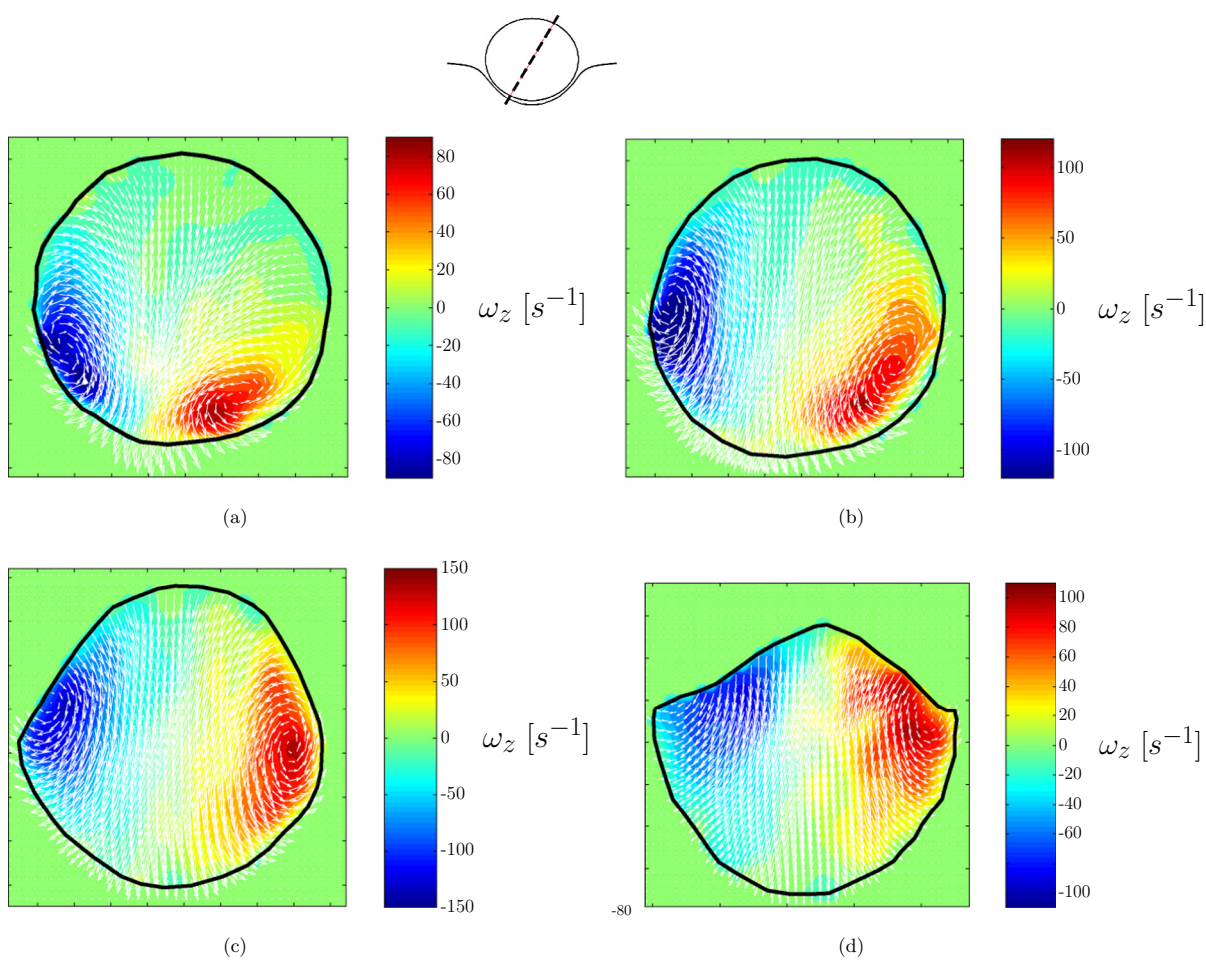

Fig. 5. Time-resolved velocity fields and contour plots of the vorticity, ω_z, in a single droplet for $\phi = 1 \times 10^{-4}$ and: (a) $t = 8$ ms; (b) $t = 16$ ms; (c) $t = 25$ ms; (d) $t = 35$ ms.

end of the coalescence. Fig. 3 shows the rupture processes for two different surfactant concentrations, $\phi = 2 \times 10^{-5}$ and $\phi = 5 \times 10^{-4}$, where the dot on each sketch indicates the initial rupture point. The solid lines indicate the interface while the dashed ones outline the volume of the fluid from the drop that is now in the bulk phase; it was possible to identify this volume because the liquid in the droplet was seeded with tracers particles and could be distinguished from the liquid in the bulk homophase.

For $\phi = 2 \times 10^{-5}$, the rupture and neck expansion proceeded quickly and ended in a short time (before 30 ms) as shown in the left column of Fig. 3. In this case, the originally flat interface does not deform significantly when the drop rests on it, and the thin film trapped between the drop and the bulk phases retracts rapidly to let the droplet merge with the bulk. During the process, the drop top surface quickly moves below the equilibrium interface and eventually reaches the quiescent state smoothly. For a mass ratio of surfactant to organic phase equal to $\phi = 5 \times 10^{-4}$, it takes longer for the droplet to coalesce with the bulk liquid, as shown in the right column of Fig. 3. In this case, the interface is significantly deformed when the drop rests on it. After the initial breakage, it takes longer for the neck to retract outwards, especially when asymmetrical rupture occurs. The upper part of the droplet does not pass through the equilibrium interface, but approaches slowly the final interface position.

The rupture time variation for different surfactant concentrations is attributed to two factors. High surfactant concentration promotes the deformation of the initially flat interface, which takes the shape of a hemisphere, and increases the length of the oil film trapped between the drop and the interface. This increases the time needed for the film to drain compared to low surfactant concentration. In addition, high surfactant concentration decreases the surface tension force that drives the expansion of the neck between the drop and the bulk fluid and the film drainage after rupture. This behavior is analogous to that reported by Yeo et al. (2003) and Nowak et al. (2016) who have shown that the presence of surfactants can have a significant effect on the drainage and stability of the organic phase film and thus on the coalescence time of drops. They reported that increased surfactant concentration slows down the film drainage and increases the coalescence time.

It was also found that the position of the initial rupture point varied. Chi and Leal (1989) investigated the film geometry (in particular the thickness of the film), using a boundary integral method, for various viscosity ratios, $\lambda = 0.1$, 1 and 10. For a low viscosity ratio, $\lambda = 0.1$, the film is thinnest at the center, and the rupture occurs at the center of the droplet, while for a high viscosity ratio, $\lambda = 10$, the film has minimum thickness at an off-axis location, where rupture would occur. Off-axis rupture on an initial flat interface has also been observed, experimentally, by other investigators. Mohamed-Kassim and Longmire (2004) reported for *Bo* number equal to 6, the location of the rupture point did not change for viscosity ratios 0.14 and 0.33. Ortiz-Dueñas et al. (2010) found that for a viscosity ratio equal to $\lambda = 0.14$ the rupture point varied with increasing Bond number. In the current work the Bond number is varied from 2.38 in the system without surfactant to 29.5 at the highest surfactant concentration system, while the viscosity ratio is constant and equal to $\lambda = 31$. For all the surfactant concentrations tested off-axis rupture was observed and, for increasing Bond number, rupture occurred further away from the on-axis

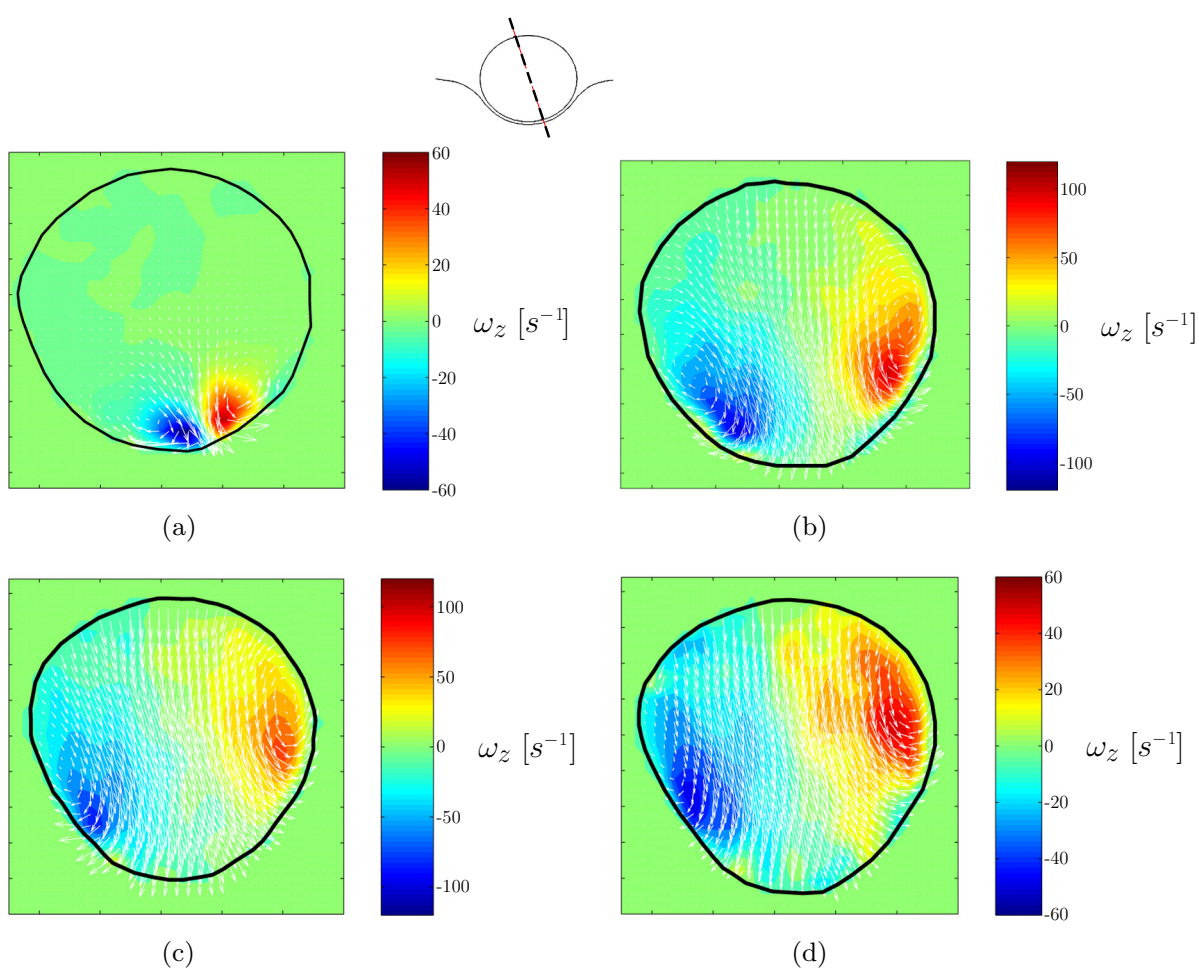

Fig. 6. Time-resolved velocity fields and contour plots of the vorticity, ω_z, in a single droplet for $\phi = 2 \times 10^{-4}$ and: (a) $t = 8$ ms; (b) $t = 30$ ms; (c) $t = 45$ ms; (d) $t = 55$ ms.

location as shown in Fig. 3. Also, for each surfactant concentration, rupture occurred at approximately the same off-axis location. It should be noted that in the current work *Bo* was varied by decreasing γ (i.e. increasing surfactant concentration). At this point, it is uncertain why the increase of the surfactant concentration causes the rupture point to be further away from the on-axis location. It is possibly due to the uneven distribution of the surfactant along the deformed interface. As reported by Ghosh and Juvekar (2002) during the drainage process, the surfactant molecules will be swept outwards by the draining film and form a ring at a distance away from the on-axis location. Therefore, the rupture location would be likely associated to the area where the surfactant molecules have the highest concentration (i.e. the lowest γ point).

The variation of the relative height from the top of the drop to the equilibrium interface, h_s, with increasing meniscus receding time, t, from the point of rupture for four different surfactant concentrations and for the case of no surfactant is shown in Fig. 4. For $t = 0$ ms, the value of h_s reduces with increasing surfactant concentration in the organic phase. As the surfactant concentration increases, the interfacial tension decreases which leads to larger deformation of the interface where the droplet is resting and reduces h_s. As the surfactant concentration approaches the CMC value, however, the rate of reduction of interfacial tension and of the interface deformation decreases. As a result, at higher surfactant concentrations the initial height h_s does not vary as much.

Immediately after rupture, h_s reduces quickly at a rate that is higher for the lower surfactant concentrations. For $\phi = 0$ and the two lowest surfactant concentrations, h_s acquires negative values which shows that the top of the drop is below the initial flat interface level. The height reaches a minimum after which it gradually approaches the equilibrium interface level. For $\phi = 0$, $\phi = 2 \times 10^{-5}$ and $\phi = 1 \times 10^{-4}$ the upper part of the droplet surface deflects at $t = 50$ ms, $t = 55$ ms and $t = 80$ ms, respectively. It is worth mentioning the maximum deflection values of the interface decreased for increasing surfactant concentration. For the higher two surfactant concentrations, the top of the drop approaches the equilibrium interface level slowly and remains positive. The time taken to reach the equilibrium interface height is much longer than in the lower surfactant concentration systems. At these high surfactant concentrations, because of the interface deformation, the film trapped between the drop and the interface takes longer to drain. In addition, the low interfacial tension reduces the surface forces which drive the expansion of the neck, which again reduces the coalescence rate.

In the current experiments, no partial coalescence was observed. As discussed in the literature, three dimensionless numbers determine the appearance of partial coalescence, Oh_1, Oh_2 and Bo_R. In the current investigation, the Ohnesorge number of the aqueous phase was $0.19 < Oh_1 < 0.68$, and for the organic phase, $0.01 < Oh_2 < 0.03$, while the Bond number based on the drop radius was $0.6 < Bo_R < 7.38$. The Oh_1 is outside the range of critical Oh_1 for partial coalescence proposed by Gilet et al. (2007) which explains why no secondary drops were seen.

3.2. Generation of the vortices inside the droplet

The evolution of the 2D time-resolved velocity fields and the contour plots of the vorticity, ω_z, after film rupture are presented for three different surfactant concentrations in this section. The results presented here are from a single droplet unless otherwise stated. In Fig. 5 the results are shown at four different time steps for $\phi = 1 \times 10^{-4}$ ($\gamma = 18.34$ mN/m). The sketch above the plots indicates the position where rupture happened. In the figure the solid line encloses the volume of the drop (volume with tracer particles) during the coalescence and should not be confused with the interface between the drop and the bulk phase. At a small time step two counter-rotating vortices are observed close to the bottom of the droplet (Fig. 5(a)). The intensity of the two vortical structures is similar in magnitude with absolute vorticity levels varying in the range of $|\omega_z| = 0$–$80\ s^{-1}$. Furthermore, for $t = 16$ ms and $t = 25$ ms (Fig. 5(b) and (c)), the two counter-rotating vortices start to move to the upper part of the droplet and their intensity increases in magnitude, with the maximum vorticity almost doubling ($|\omega_z| = 80$–$150\ s^{-1}$). During these times (Fig. 5(b) and (c)), the droplet shape changes from spherical to elliptical while sharp angles start to appear on either side of the droplet. For $t = 35$ ms (Fig. 5 (d)), a transition occurs in the velocity vector field, and a downward axial motion dominates the flow dynamics inside the droplet.

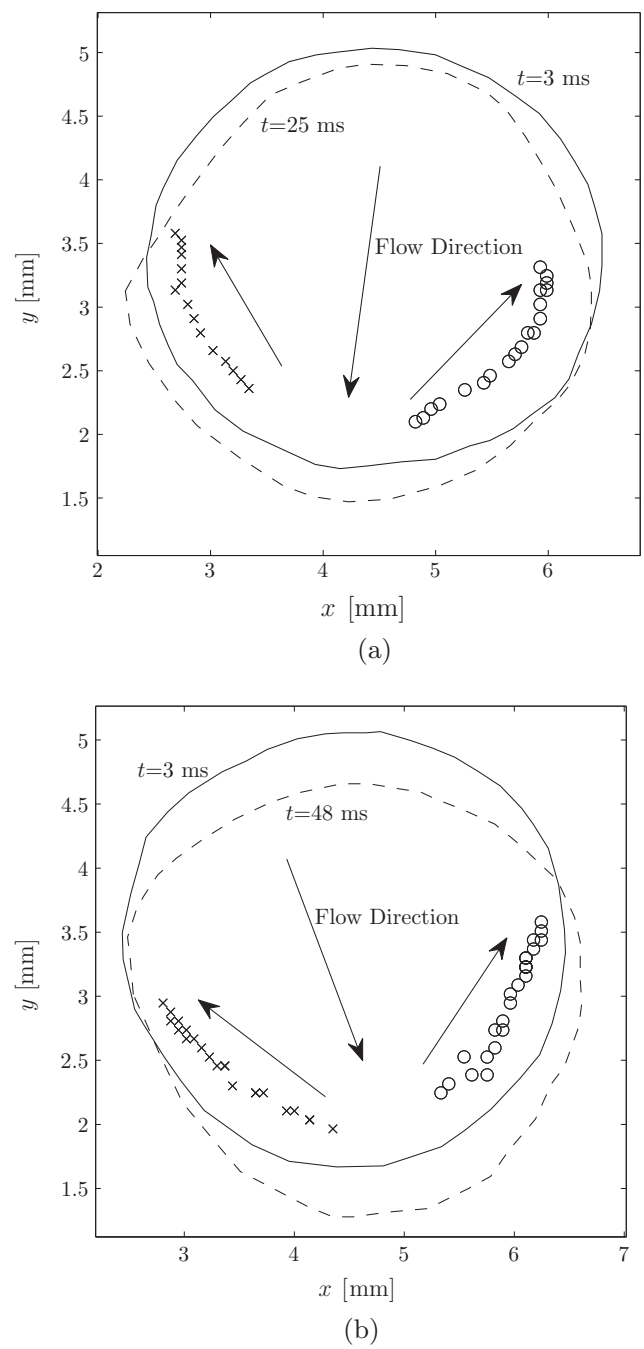

Fig. 7. Spatial evolution of the centers of the two vortices present on the left (×) and right (∘) hand side in a single droplet for: (a) $\phi = 1 \times 10^{-4}$; (b) $\phi = 2 \times 10^{-4}$.

Despite the presence of this strong downward axial motion, the two vortical structures, in the upper part of the droplet, are still identifiable. In addition, the areas occupied by the two counter-rotating vortices are of similar magnitude throughout the coalescence process. The results are consistent with the findings of Mohamed-Kassim and Longmire (2004), who have shown from vorticity counter plots for varying viscosity ratio, $\lambda = \mu_d/\mu_s = 0.14$ and 0.33, and constant interfacial tension, $\gamma = 29$ mN/m, that two counter-rotating vortices first appeared at the bottom of the droplet which stayed attached to the sides and moved to the upper part of the droplet as coalescence progressed.

The time-resolved velocity field and vorticity contour plots for mass ratio $\phi = 2 \times 10^{-4}$ ($\gamma = 9.56$ mN/m) are shown in Fig. 6(a)–(d). Similar to the previous case, two counter-rotating vortices can be distinguished in all the plots. As t increases (Fig. 6(a)–(d)), the two counter-rotating vortices move from the bottom of the drop to the upper part and their intensity increases in magnitude, with the maximum dimensional vorticity increasing more than tenfold ($|\omega_z| = 10$–$110\ s^{-1}$). While in the beginning the two vortices only occupy a small part of the drop, at $t = 30$ ms and 45 ms, they extend over the entire droplet (Fig. 6(b) and (c)) and completely control the flow dynamics inside it. At time $t = 55$ ms, a transition occurs and a downward axial motion dominates the flow dynamics inside the droplet (Fig. 6(d)). Compared to $\phi = 1 \times 10^{-4}$, the flow transition occurred at a later time for $\phi = 2 \times 10^{-4}$, while the droplet shape remained almost spherical during the whole time. As was discussed before, the presence of surfactants increases the coalescence time.

The motion and trajectory of the two counter-rotating vortices are summarized in Fig. 7 for the two surfactant concentrations,

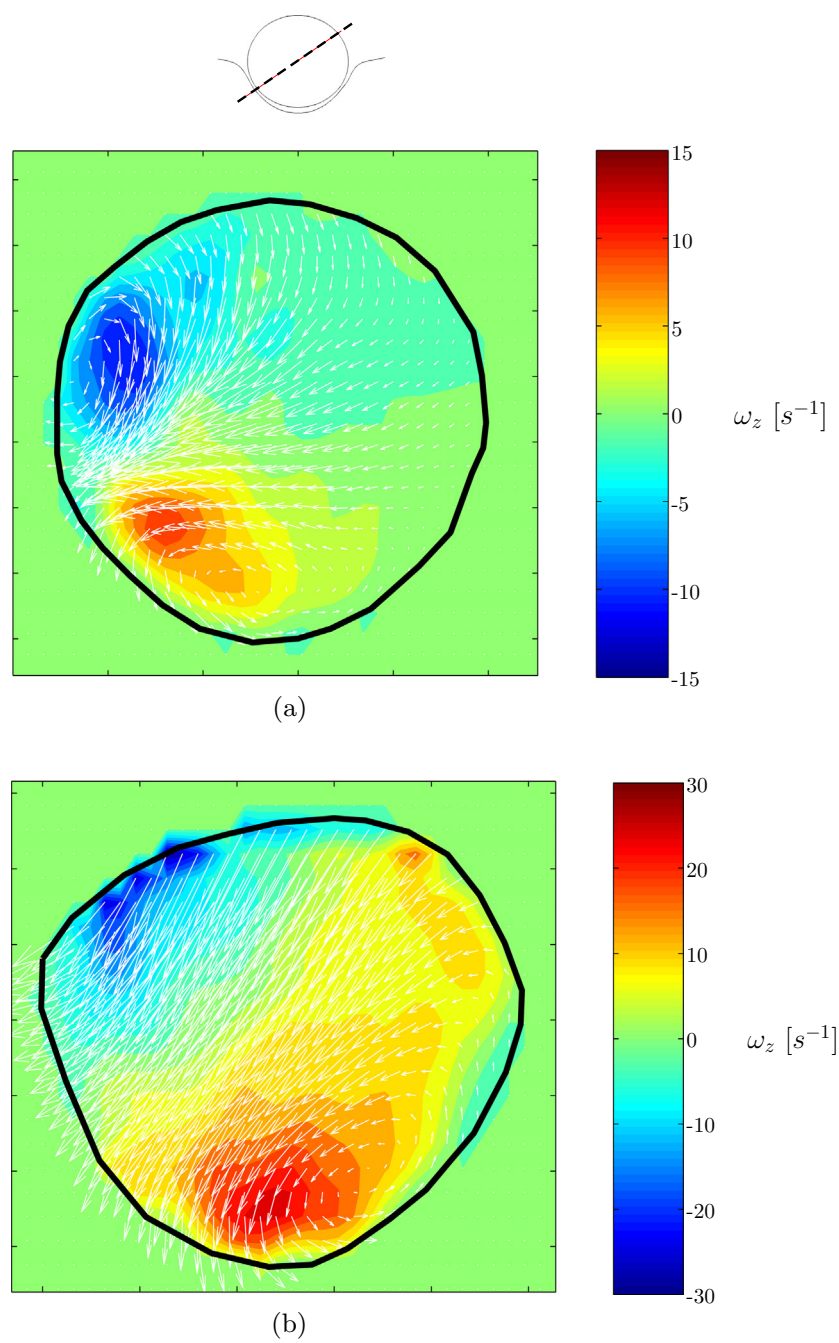

Fig. 8. Time-resolved velocity fields and contour plots of the vorticity, ω_z, in a single droplet for $\phi = 5 \times 10^{-4}$ and: (a) $t = 8$ ms; (b) $t = 70$ ms.

where the x and y coordinates of the vortex centers are tracked over time. Due to the resolution of the velocity field, the cores of the vortices cannot be observed until $t = 3$ ms. When the vortices move close to the upper surface of the droplet, they are suppressed and their full shape cannot be recognized. At this time the recording is terminated (for $\phi = 1 \times 10^{-4}$, $t = 25$ ms and for $\phi = 2 \times 10^{-4}$, $t = 48$ ms). The solid lines show the shape of the droplet when the two counter-rotating vortices first appear, while the dashed lines indicate the shape of the droplet when the vortices have disappeared. It is evident from the schematic diagrams in Fig. 7(a) and (b) that the cores of the vortices originate from the film rupture point at the bottom of the droplet. For increasing receding time, t, the centers of the vortices stay attached to the sides of the droplet. For low surfactant concentration, $\phi = 1 \times 10^{-4}$, the vortices propagate faster to the upper part of the droplet and travel over a longer distance compared to the higher surfactant concentration system.

The velocity vector and vorticity fields for the high mass ratio of surfactant to organic phase, $\phi = 5 \times 10^{-4}$ are shown in Fig. 8. Similar to the lower surfactant concentrations, at short times (Fig. 8(a), $t = 8$ ms) two counter rotating vortices of similar magnitude appear on each side of the rupture point. However, at longer times (Fig. 8 (b), $t = 70$ ms) a significant change is observed and the vortical structures become asymmetric. This difference is attributed to the location of the rupture point. For this concentration, the film rupture occurred off-center and near the equilibrium interface height, while for $\phi = 1 \times 10^{-4}$ and $\phi = 2 \times 10^{-4}$ rupture occurred near the center of the deformed interface. When asymmetric rupture occurs, such as the one shown in Fig. 8, it takes longer for the oil film to retract outwards on one side of the droplet compared to the side closest to the equilibrium interface height, which causes the difference in the flow pattern within the drop.

A further analysis was carried out to assess how the circulation of the two counter-rotating vortices varied with the receding time, t. The circulation, $\Gamma_{\omega_z^*}$, was estimated from Eq. (2) where the integral was carried out over the area, A_ω, which corresponds to a vorticity level $\omega_z > 10\ \mathrm{s}^{-1}$. A visualization of the areas $A_{\omega R}$ and $A_{\omega L}$ for the right and left hand side vortices, respectively, is shown in Fig. 9(a).

$$\Gamma_{\omega_z^*} = \frac{\int_{A_\omega} |\omega_z| dA_\omega}{A_\omega} \tag{2}$$

The circulation, $\Gamma_{\omega_z^*}$, for $\phi = 2 \times 10^{-4}$ of the right and left hand side vortices is shown in Fig. 9(b) for a single droplet. As can be seen the circulations of the two vortices at either side of the rupture point are of comparable magnitude for the whole time studied. It can also be noted that the greatest circulation, $\Gamma_{\omega_z^*}$, is observed for 14 ms $< t <$ 30 ms, where the intensity of the vorticity is high and the vortices occupy most of the droplet. For $t <$ 14 ms the vortices have just started forming and are restricted to the lower part of the drop, while for $t >$ 30 ms the flow inside the drop becomes dominated by the downward axial motion.

The effect of surfactant concentration on $\Gamma_{\omega_z^*}$ averaged over 10 drop coalescence events is shown in Fig. 9(c) for $\phi = 1 \times 10^{-4}$, $\phi = 2 \times 10^{-4}$ and $\phi = 5 \times 10^{-4}$. It should be noted that the rupture points chosen for averaging $\Gamma_{\omega_z^*}$ were of the same proximity from the center point of the deformed interface in order to obtain comparable flow fields. Since in all cases the two counter-rotating vortices are symmetrical, the circulations of one of the vortical structures are only presented. Again the calculations were carried out for iso-vorticity levels $\omega_z > 10\ \mathrm{s}^{-1}$. The iso-vorticity contour $\omega_z > 10\ \mathrm{s}^{-1}$ was selected because it can capture the vortices from the beginning of the coalescence. For example, the minimum iso-vorticity contour observed for $\phi = 1 \times 10^{-4}$ at $t = 1$ ms is $\omega_z = 10\ \mathrm{s}^{-1}$, while for $\phi = 5 \times 10^{-4}$ an iso-vorticity contour, $\omega_z = 10\ \mathrm{s}^{-1}$, is observed at $t = 7$ ms. As can be seen $\Gamma_{\omega_z^*}$ increases with decreasing ϕ. For $t <$ 14 ms similar circulation levels are observed for $\phi = 1 \times 10^{-4}$ and $\phi = 2 \times 10^{-4}$, while for 14 ms $< t <$ 30 ms the circulation levels for $\phi = 1 \times 10^{-4}$ ($\Gamma_{\omega^*_{zmax}} = 48\ \mathrm{s}^{-1}$) are higher than those for $\phi = 2 \times 10^{-4}$ ($\Gamma_{\omega^*_{zmax}} = 35\ \mathrm{s}^{-1}$) and $\phi = 5 \times 10^{-4}$ ($\Gamma_{\omega^*_{zmax}} = 16\ \mathrm{s}^{-1}$). For all the γ investigated, a plateau of the $\Gamma_{\omega_z^*}$ is reached, which indicates that the counter-rotating vortices have extended over the entire droplet when their intensities have reached a maximum. The plateau extends to longer times as the surfactant concentration increases, indicating that for high ϕ the counter-rotating vortices spread over the entire droplet over a longer period compared to a low ϕ. For

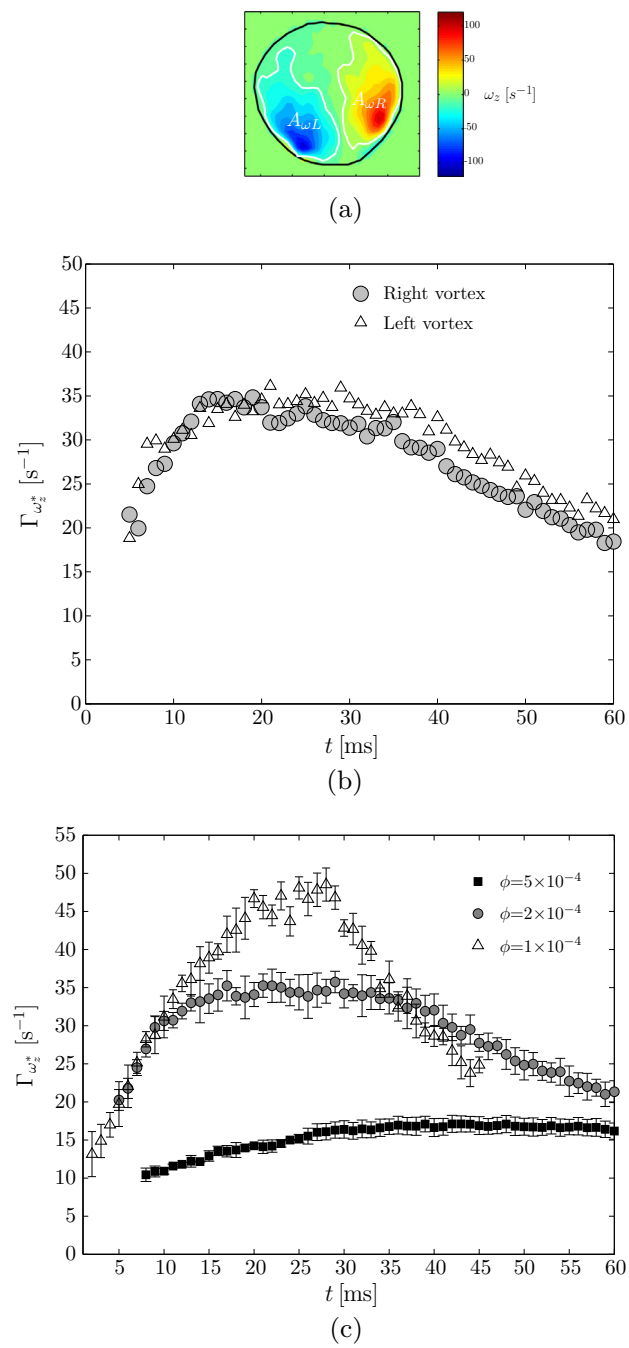

Fig. 9. (a) Visualization of the area, $A_{\omega_z^*}$, over which the circulation $\Gamma_{\omega_z^*}$ has been estimated ($\phi = 2 \times 10^{-4}$); (b) variation of the dimensional circulation, $\Gamma_{\omega_z^*}$, with increasing t for both the right and left hand side vortices ($\phi = 2 \times 10^{-4}$) in a single droplet; (c) variation of the dimensional circulation, $\Gamma_{\omega_z^*}$, with increasing t for different ϕ, averaged over 10 droplets.

$\phi = 1 \times 10^{-4}$ and $\phi = 2 \times 10^{-4}$ the $\Gamma_{\omega_z^*}$ decreases after times $t = 30$ ms and $t = 40$ ms, respectively. Beyond these times a transition occurs in the flow pattern and a downward axial motion dominates the flow dynamics inside the droplet. At the high surfactant concentration, $\Gamma_{\omega_z^*}$ increases slightly and then remains almost constant which agrees with the slow dynamics of the neck evolution that result in low intensity vortices.

3.3. Kinetic energy per unit mass

The kinetic energy per unit mass contour plots of Fig. 10 allow a quantitative comparison of the velocity dynamics inside the droplet for different mass ratio of surfactant to organic phase at different time instants during the coalescence. It should be noted that the kinetic energy per unit mass of Fig. 10 has been estimated according to the two dimensional approximation of Eq. (3), where the indices x and y refer to the velocity components measured in the plane considered, while the third component contribution is estimated as the average of the other two (i.e. $w^2 = 0.5(u^2 + v^2)$).

$$k_{xy} = \frac{3}{4}(u^2 + v^2) \tag{3}$$

The kinetic energy per unit mass, k_{xy}, inside the droplet for $\phi = 1 \times 10^{-4}$ and $\phi = 2 \times 10^{-4}$, is shown in Fig. 10(a, b) and (c, d), respectively, for different time steps. At the initial stages of coalescence k_{xy} is mainly distributed near the bottom of the droplet (see Fig. 10(a) and (c)). Prior to rupture, the fluid inside the droplet is motionless. Once the film separating the drop and the interface reaches a critical thickness (Chen, 1985), rupture occurs at the lower part of the droplet. All the fluid situated near the bottom of the droplet rushes through the rupture point as shown in the kinetic energy per unit mass distribution. At the later stages of coalescence, the k_{xy} is mainly distributed near the top of the droplet (Fig. 10(b) and (d)). At these stages a combination of gravity and interfacial tension forces push the fluid at the top of the drop downwards, generating a strong axial flow (see also Figs. 5(d) and 6(d)). It should be noted that at high ϕ, the interfacial tension is reduced, and the intensity of k_{xy} inside the droplet is also reduced as shown in Fig. 10(c) and (d). Furthermore, the patterns of the two counter-rotating vortices described previously in Section 3.2, are a result of the high momentum imparted to the fluid by the fast downward motion of the droplet in conjunction with the rapidly growing neck. These two effects force the fluid to follow a circular motion along a closed loop inside the drop (see Fig. 5(a)–(c)). For low ϕ, a fast growth of the neck is expected (Aarts et al., 2005; Lu and Corvalan, 2012; Chinaud et al., 2016) which, in combination with high k_{xy} (see Fig. 10(a) and (b)) in the center of the droplet, results in high intensity vortical structures. At high ϕ, or

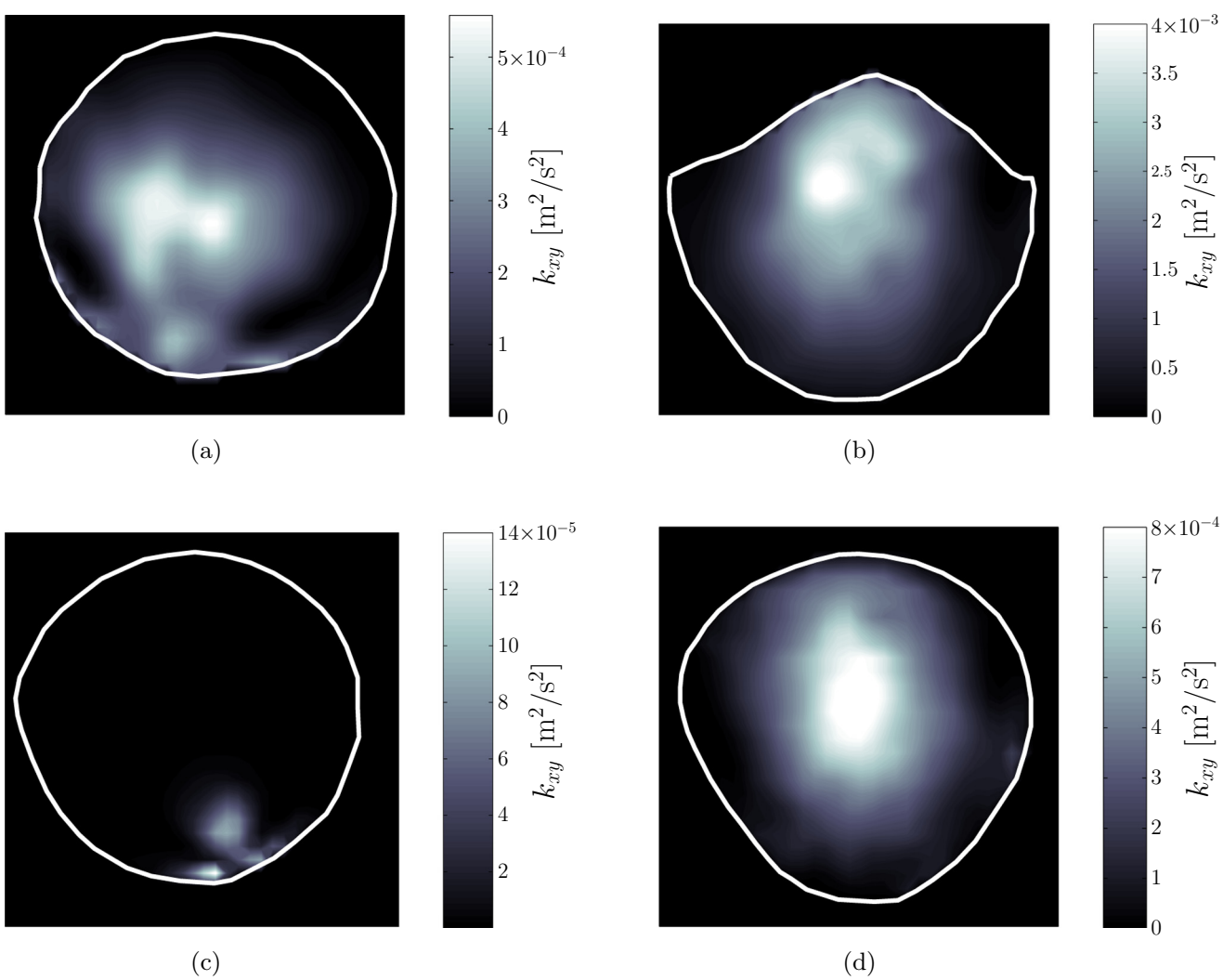

Fig. 10. Contour plots of the kinetic energy per unit mass, k_{xy}, in a single droplet for: (a) $\phi = 1 \times 10^{-4}$ and $t = 8$ ms; (b) $\phi = 1 \times 10^{-4}$ and $t = 35$ ms; (c) $\phi = 2 \times 10^{-4}$ and $t = 8$ ms; (d) $\phi = 2 \times 10^{-4}$ and $t = 55$ ms.

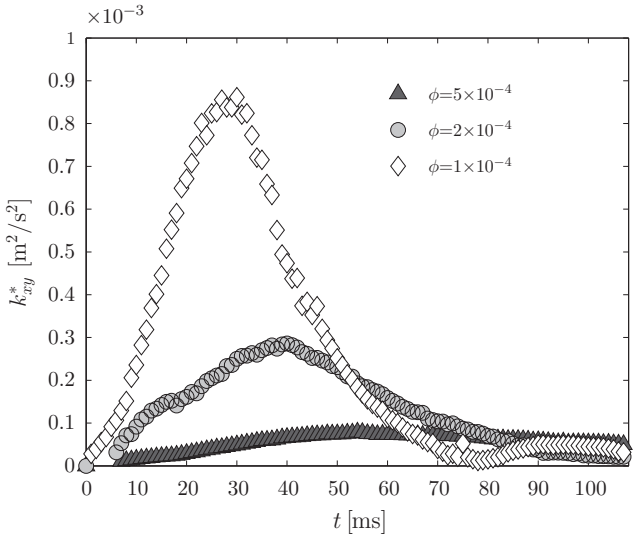

Fig. 11. Variation of the space-averaged kinetic energy per unit mass, k^*_{xy}, in a single droplet with increasing t for different ϕ.

low interfacial tension force, k_{xy} and the velocity of the neck growth of the droplet are reduced and therefore decrease the intensity of the vortices inside the droplet.

The variation of the space-averaged kinetic energy per unit mass over the measurement plane in the drop, k^*_{xy}, with receding time, t, is calculated from Eq. (4).

$$k^*_{xy} = \frac{1}{A}\int_A k_{xy} dA \tag{4}$$

The results are shown in Fig. 11 for $\phi = 1 \times 10^{-4}$, $\phi = 2 \times 10^{-4}$ and $\phi = 5 \times 10^{-4}$. As already discussed, at a receding time $t = 0$ ms, the fluid inside the droplet is motionless and k^*_{xy} has its lowest value. As t increases k^*_{xy} gradually increases and peaks at $t = 28$ ms for $\phi = 1 \times 10^{-4}$ ($k^*_{xy} = 8.8 \times 10^{-4}$ m^2 s^{-2}), $t = 39$ ms for $\phi = 2 \times 10^{-4}$ ($k^*_{xy} = 2.9 \times 10^{-4}$ m^2 s^{-2}) and $t = 56$ ms for $\phi = 5 \times 10^{-4}$ ($k^*_{xy} = 9 \times 10^{-5}$ m^2 s^{-2}). After the peaks, k^*_{xy} decreases for all the ϕ investigated. For $\phi = 1 \times 10^{-4}$, k^*_{xy} reaches a value of zero at $t = 80$ ms and thereafter it increases again. This is related to the behavior of the interface for this surfactant concentration. As shown in Fig. 4, the interface reaches its maximum downward deflection at this time and then moves upwards to its equilibrium position. Conversely, for $\phi = 2 \times 10^{-4}$ and $\phi = 5 \times 10^{-4}$ the values of k^*_{xy} decrease to zero when complete coalescence of the droplet occurs.

4. Conclusions

In the paper the effect of an oil soluble surfactant on the coalescence of a drop with a liquid/liquid interface was investigated. The shape of the interface while the droplet rested on it was studied with a PIV system before the thin film that separated the drop from the interface ruptured. It was found that prior to rupture the interface under the droplet deformed while the deformation increased with increasing surfactant concentration. In addition, as the surfactant concentration increased, the time needed for the film to drain and rupture to occur also increased. The interface behavior during coalescence was similar to that observed in previous experiments on drops rupturing at liquid/liquid interfaces (Mohamed-Kassim and Longmire, 2004). A key difference, however, is that in the current experiments, no deflection of the interface was observed during coalescence at high surfactant concentrations in the organic phase. Under all the conditions considered, no partial coalescence was observed.

The high speed PIV system was also utilized to obtain the velocity fields, the evolution of the vortices and the kinetic energy per unit mass distribution inside the droplet after the film rupture. Immediately after rupture, two counter-rotating vortices appeared at the bottom of the droplet on either side of the rupture point, which then moved towards the upper part of the droplet while their corresponding intensities increased. At a later stage, a transition occurred and the dynamics in the droplet were no longer dominated by the two counter-rotating vortices but by a downward axial motion. After the transition, the intensities of the vortices decreased with time. With increasing surfactant concentration the intensity of the two counter rotating vortices decreased. The kinetic energy per unit mass, k_{xy}, distribution inside the droplets for different surfactant concentrations was calculated from the velocity fields. At the early stages of coalescence, k_{xy} was mainly distributed near the bottom part of the droplet, while in the later stages of the coalescence it was distributed near the upper part of the droplet.

These results will form the basis for future investigations on the effect of different surfactants on drop coalescence. They will also provide the detailed hydrodynamic information needed for the development and validation of numerical models on coalescence.

Acknowledgements

This project was funded by the UK Engineering and Physical Sciences Research Council (EPSRC) Programme Grant MEMPHIS. The authors would like to acknowledge the EPSRC Instrument Pool for the loan of the high-speed camera. Teng Dong would also like to thank the Chinese Scholarship Council (CSC) for providing his studentship.

References

Aarts, G., Lekkerkerker, H.N., 2008. Droplet coalescence: drainage, film rupture and neck growth in ultralow interfacial tension systems. J. Fluid Mech. 606, 275–294.
Aarts, G., Lekkerkerker, N., Guo, H., Wegdam, G.H., Bonn, D., 2005. Hydrodynamics of droplet coalescence. Phys. Rev. Lett. 95, 164503.
Blanchette, F., Messio, L., Bush, J., 2009. The influence of surface tension gradients on drop coalescence. Phys. Fluids, 21.
Blawzdziewicz, J., Cristini, V., Loewenberg, M., 1999. Near-contact motion of surfactant-covered spherical drops: ionic surfactant. J. Colloid Interface Sci. 211, 355–366.
Bordoloi, A., Longmire, E., 2012. Effect of neighboring perturbations on drop coalescence at an interface. Phys. Fluids, 24.
Charles, G., Mason, S., 1960. The coalescence of liquid drops with flat liquid/liquid interfaces. J. Colloid Sci. 15, 236–267.
Chen, J., 1985. A model of coalescence between two equal-sized spherical drops or bubbles. J. Colloid Interface Sci. 107, 209–220.
Chi, B., Leal, L., 1989. A theoretical study of the motion of a viscous drop toward a fluid interface at low Reynolds number. J. Fluid Mech. 201, 123–146.
Chinaud, M., Voulgaropoulos, V., Angeli, P., 2016. Surfactant effects on the coalescence of a drop in a Hele-Shaw cell. Phys. Rev. E, 94.
Dai, B., Leal, L., 2008. The mechanism of surfactant effects on drop coalescence. Phys. Fluids, 20.
Dalgleish, D., 1997. Adsorption of protein and the stability of emulsions. Trends Food Sci. Technol. 8, 1–6.
Eri, A., Okumura, K., 2010. Bursting of a thin film in a confined geometry: rimless and constant-velocity dewetting. Phys. Rev. E, 82.
Ghosh, P., Juvekar, V., 2002. Analysis of the drop rest phenomenon. Chem. Eng. Res. Des. 80, 715–728.
Gilet, T., Mulleners, K., Lecomte, J., Vandewalle, N., Dorbolo, S., 2007. Critical parameters for the partial coalescence of a droplet. Phys. Rev. E, 75.
Kavehpour, H.P., 2015. Coalescence of drops. Annu. Rev. Fluid Mech. 47, 245–268.
Liao, Y., Lucas, D., 2010. A literature review on mechanisms and models for the coalescence process of fluid particles. Chem. Eng. Sci. 65, 2851–2864.
Lu, J., Corvalan, C.M., 2012. Coalescence of viscous drops with surfactants. Chem. Eng. Sci. 78, 9–13.

Malmazet, E., Risso, F., Masbernat, O., Pauchard, V., 2015. Coalescence of contaminated water drops at an oil/water interface: influence of micro-particles. Colloids Surf. A: Physicochem. Eng. Aspects 482, 514–528.
Martin, D.W., Blanchette, F., 2015. Simulations of surfactant effects on the dynamics of coalescing drops and bubbles. Phys. Fluids, 27.
Mohamed-Kassim, Z., Longmire, E., 2004. Drop coalescence through a liquid/liquid interface. Phys. Fluids 16, 2170–2181.
Neitzel, G., Dell'Aversana, P., 2002. Noncoalescence and nonwetting behavior of liquids. Annu. Rev. Fluid Mech. 34, 267–289.
Nowak, E., Kovalchuk, N.M., Che, Z., Simmons, M.J.H., 2016. Effect of surfactant concentration and viscosity of outer phase during the coalescence of a surfactant-laden drop with a surfactant-free drop. Colloids Surf. A: Physicochem. Eng. Aspects 505, 124–131.
Ortiz-Dueñas, C., Kim, J., Longmire, E.K., 2010. Investigation of liquid–liquid drop coalescence using tomographic PIV. Exp. Fluids 49, 111–129.
Paul, E., Atiemo-Obeng, V.A., Kresta, S.M., 2004. Handbook of Industrial Mixing: Science and Practice. John Wiley & Sons, Inc.
Samanta, S., Ghosh, P., 2011. Coalescence of air bubbles in aqueous solutions of alcohols and nonionic surfactants. Chem. Eng. Sci. 66, 4824–4837.
Thoroddsen, S., Takehara, K., 2000. The coalescence cascade of a drop. Phys. Fluids 12, 1265–1267.
Yeo, L.Y., Matar, O.K., de Ortiz, E.S.P., Hewitt, G.F., 2003. Film drainage between two surfactant-coated drops colliding at constant approach velocity. J. Colloid Interface Sci. 257, 93–107.